X-ray radioscopic visualization of bubbly flows injected through a top submerged lance into a liquid metal

Akashi, M.; Keplinger, O.; Anders, S.; Shevchenko, N.; Reuter, M.; Eckert, S.;

Originally published:

October 2019

Metallurgical and Materials Transactions B 51B(2019), 124-139

DOI: https://doi.org/10.1007/s11663-019-01720-y

Perma-Link to Publication Repository of HZDR:

https://www.hzdr.de/publications/Publ-29137

X-ray radioscopic visualization of bubbly flows injected through a top submerged lance into a liquid metal

Megumi AKASHI[1], Olga KEPLINGER, Natalia SHEVCHENKO, Sten ANDERS, Markus REUTER, Sven ECKERT

Helmholtz Zentrum Dresden-Rossendorf (HZDR), Bautzner Landstraße 400, 01328 Dresden, Germany

[1] corresponding author: m.akashi@hzdr.de

Abstract

We present an experimental study on the formation and behaviour of a liquid metal bubbly flow arising from a downward gas injection through a top submerged lance (TSL). A visualization of the bubble dynamics was achieved by the X-ray radiography combined with high-speed imaging. The experiments were carried out in a parallelepiped container (144×144×12 mm^3) using GaInSn, a ternary alloy that is liquid at room temperature. The gas flow rate Q_{gas} was adjusted in a range between 0.033 and 0.1 l/s. Three different injection positions were considered with respect to the submergence depth L. X-ray images allow for a characterization of the flow regimes and provide the properties of the individual bubbles such as size, shape and trajectory. Formation and entrainment of smaller gas bubbles are observed at the free surface. These small bubbles can be trapped in the fluid for a long time by recirculation vortices. Bubbles size distributions are determined for different Q_{gas}. The bubble detachment frequency is measured as a function of Q_{gas} and L. The results are compared with previously published data for water. The X-ray radiography offers an effective method for determining the local void fraction and allows for an estimation of the bubble volume.

I. Introduction

Since the emergence of first ideas and concepts about 50 years ago, the TSL (top submerged lance) process has become an essential component of the non-ferrous metallurgical industry.[1] The process, which is characterized by blowing reactive gas through the submerged lance into a liquid slag bath, is applied for waste treatment, E-Waste recycling or the production of several metals such as tin, copper, nickel, lead, platinum group elements, or zinc. The gas injection nozzle is designed as a straight lance which is aligned vertically and is immersed in the liquid bath from above. The attractiveness of the TSL process results from the simple configuration, the robustness and the variability of the operating conditions. The process can be readily controlled by variations of the gas composition, the gas flow rate or the submergence depth of the lance in the bath. The productivity of the reactor is determined by the efficiency of the chemical reaction between the gas (or solid particles transported in it) and the liquid. Achieving a high reaction rate requires an excellent exchange between the phases and therefore a large interface. This, in turn, varies greatly with the number and size of gas bubbles formed on the nozzle or the extent of splashing on the free surface. Obviously, the degree of turbulence in the bath plays a decisive role here. For this reason, it is obvious that the design of an efficient TSL process requires a profound knowledge of the fluid dynamic conditions taking into account complex multiphase flows.

Over the years, a number of experimental and numerical studies focusing on flow behavior in the TSL process have been performed. Igwe *et al.* [2] studied the nitrogen gas injection into a water bath through different nozzle types. The authors suggested empirical relationships concerning the penetration of the gas jet into the liquid phase and qualitatively described the bubble dispersion and the splashing behavior. Mazumdar & Guthrie [3] developed a steady-state, turbulent flow model for various axisymmetric configurations of gas injection systems (including TSL) used in ladle refining. A satisfying quantitative

agreement between predicted flow fields and a reduced scale water model was achieved. Iguchi *et al.* [4] considered the possibility that the gas injection through a top submerged lance can create a swirling motion in the liquid. It is feared that such rotational bath movement in a metallurgical reactor can lead to uncontrolled flow conditions causing erosion of the wall material. The swirling motion starts when the gas flow rate exceeds a certain value. This onset can be delayed by adjusting a deeper immersion of the lance in the fluid. Experiments were performed in water, aqueous glycerol solution, mercury and Wood's metal. On the basis of the experimental data, the vertical migration distance of a bubbling jet were given by the empirical equation as a function of the modified Froude number. These findings were clarified and refined by more recent water experiments.[5] Another experimental study dealing with the submerged lance injection process was published by Gosset *et al.* [6] The bubbling frequency at the downward facing nozzle was measured for variations of the gas flow rate, the lance diameter and the submergence depth. A related dimensionless correlation is suggested in terms of the bubble Strouhal number and the ratio of the Weber and the Bond number.

Driven by the objective to improve the efficiency of the process by achieving a higher reaction rate, the effect of a cross-flow on the bubble formation at a downward-facing single-hole nozzle has been investigated by Goda *et al.* [7] Here, the cross-flow was generated by rotating the cylindrical vessel around its vertical axis. The measurements demonstrated that the frequency of bubble formation increases with growing rotational velocity.

Morsi *et al.*[8] performed experiments using a lance design which resembles the so-called SIROSMELT lance which is applied in industrial extractive metallurgy. [1] This lance consists of two coaxial steel pipes. While the inner tube serves to convey reactants into the reactor, oxygen-enriched air is blown through the outer cylindrical gap into the fluid. It was found that it is beneficial to generate a swirl component for the gas flow in the annulus. A strong swirling flow increases the turbulence and enhances the heat transfer. [8,9] The latter ensures a better cooling of the lance and, consequently, a longer lifetime.

A CFD model for TSL gas injection was introduced by Huda *et al.* [10] and validated against the air-water experiment carried out by Morsi *et al.* [8] The authors suggest a certain submergence depth of the lance to achieve a better mixing and a higher turbulence level in the liquid. A swirling gas injection increases the mixing near the lance tip. Furthermore, a large-scale recirculation has to be formed in the liquid bath for achieving uniform mixing, but, the recirculation regions were found to be weak considering the water case. The CFD model was extended and applied to the zinc fuming process. [11] The predicted zinc fuming rate was compared with data available from pilot plant trials. A numerical study of ladle stirring by top and bottom gas injection was reported by Torres & Barron. [12] The simulations showed that the bottom gas injection leads to a higher mixing efficiency as the submerged lance injection. The mixing efficiency for the submerged lance injection increases with increasing both the gas flow rate and the lance submergence depth.

Despite previous work in this field, accurate prediction of reaction kinetics in the real process remains an extremely difficult and largely unsolved task. The efficiency of the TSL process is largely determined by the fluid dynamics and the spatial structure of complex multiphase flows at high gas contents. Numerical calculations of these flows with the additional option of chemical reactions are quite complex and not feasible until today without adequate modeling. Corresponding accurate experimental data, which are characterized by a high spatial and temporal resolution and are therefore suitable for validation of the numerical models, can be obtained only with great effort and hardly exists for liquid metals until today. Many experimental studies rely on water models. However, significant differences regarding the properties of liquid metals such as density, viscosity and surface tension lead to discrepancies in essential non-dimensional parameters as the bubble Reynolds number, the Weber number or the Morton number. In particular, the higher surface tension of liquid metals tends to reduce the deformation of the bubble and the bubble size. [13] Moreover, liquid metal bubbly flows show a high rate of bubble collision and subsequent coalescence. [14,15] For a horizontal gas injection into mercury Oryall & Brimacombe [16] observed an extremely rapid expansion of gas jets upon discharge from the nozzle being significantly higher as found for air jets in water.

Usually a lance blows into a slag in TSL furnace. This study is a first step towards a physical modeling of the TSL slag blowing and presents experimental investigations of the bubbly flow regime arising from a downward gas injection through a top submerged lance into a liquid metal. In the future the viscosity will be modified to emulate TSL slag blowing. X-ray radiography in combination with high speed imaging is applied as a diagnostic technique to visualize the motion and dispersion of the gas bubbles. Experimental data with respect to the bubble frequency, bubble area and void fraction are obtained by image processing. The main focus of this work lies on the formation and the behaviour of particular bubbles at different gas flow rates and submergence depths of the nozzle. Ultimately, these results will be used to calibrate CFD models of TSL furnaces.

II. Experimental Setup

A. *Apparatus*

The experiments were carried out in the X-ray laboratory at HZDR. The experimental configuration is almost identical to the measuring arrangement developed by Keplinger *et al.* [13,14] for investigating the behavior of bubble plumes generated by bottom gas injection. The ternary alloy GaInSn was used as a model fluid whose eutectic composition ($Ga^{67}In^{20.5}Sn^{12.5}$) is liquid at room temperature. A compilation of essential thermophysical properties measured in a wide temperature range was reported by Plevachuk *et al.* [17] In particular, the low viscosity (ν_l = 3.4×10^{-7} m^2/s), the high density (ρ_l = 6360 kg/m^3) and the high surface tension (σ_l = 0.533 N/m) result in very low values of the Morton number Mo = 2×10^{-13}. Figure 1 shows schematic drawings of the experimental setup, the vessel and the positions of the gas injection nozzle. The liquid metal was filled up to a height of H = 144 mm into a narrow vessel made of acrylic glass with a horizontal rectangular cross section of 144×12 mm^2 (see Figure 1(b)). The high attenuation of X-ray radiation in the liquid metal and the dynamics of the bubble motion restrict the dimension of the fluid container along the X-ray beam. Images with good intensity contrast and low signal-to-noise ratio can only be achieved by using such a flat geometry. Previous measurements [13,14,18] have shown that a gap of D = 12 mm is a good compromise to obtain a clear visualization of the bubbles and the gas-liquid interfaces on the one hand and on the other hand to allow sufficient dynamics of both the bubble plume and the free surface of the melt. The acrylic glass used as the wall material does not cause any significant attenuation of the X-ray beam intensity.

The inert gas Argon (density ρ_g = 1.78 kg/m^3 and viscosity ν_g = 1.25×10^{-5} m^2/s) is injected through a straight lance made of stainless steel having an outer diameter of d_{out} = 5.5 mm and an inner diameter of d_{in} = 5.0 mm. A gas flow control system (MKS Instruments) is used to vary the gas flow rate in a range from 2000 cm^3/min to 6000 cm^3/min (Q_{gas} = 0.033 … 0.1 l/s). The system is normed to Nitrogen at standard conditions (1bar, 0°C). Thus, the desired gas flow is adjusted by applying a correction factor. The lance was aligned vertically and immersed in the melt from above at the centre of the container's horizontal cross-section. Three injection positions have been chosen with different submergence depths L: L = 1/4 H (top), 1/2 H (middle) and 3/4 H (bottom).

The applicability of X-ray radiography for quantitative measurement of bubble parameters rising in a stagnant liquid was already validated by previous studies. [13] A high power X-ray source (ISOVOLT 450M1/25-55 from GE Sensing & Inspection Technologies GmbH) operating with a maximum voltage of 320 kV and a current of 14 mA generates a divergent polychromatic X-ray beam. A scintillation screen (SecureX HB from Applied Scintillation Technologies) is attached to the surface of the container as shown in Figure 1(a). It converts the fraction of the X-ray beam, which is not absorbed within the fluid container, into visible light. The further imaging is completed with a lens system (Thalheim – Spezial – Optik) and a high-speed video camera (Pco.edge from PCO) equipped with a sCMOS-sensor. The images were captured with a frequency of 125 frames per second (fps) and an exposure time of 3 milliseconds. The exposure time was optimized to achieve a good signal-to-noise ratio together with a low in-motion blurring caused by the bubbles high rising velocities. The measurement time was 40 seconds starting with the initiation of the bubble injection. In all experiments presented here the size of the observation window was approximately 116×172 mm^2 (1730×2560 px^2) as shown in Figure 1(b) yielding a spatial resolution of each pixel of l_{px} = 0.067 mm. The difference between the very high attenuation of X-ray radiation of the liquid

metal and the extremely weak attenuation of Argon leads to a clear contrast in the resulting images. The local image intensity thereby correlates with the fraction of gas at a specific position in the *y*-*z*-plane. The quantitative analysis of bubble parameters is performed by means of digital image processing. The fact that large parts of the volume in the fluid vessel, which are above the free surface, are almost completely filled with gas (with the exception of a few small liquid metal droplets) would lead to a strong overexposure of the recordings. To prevent this, this zone was covered with a thin lead foil and the corresponding image area is not taken into account in the quantitative analysis.

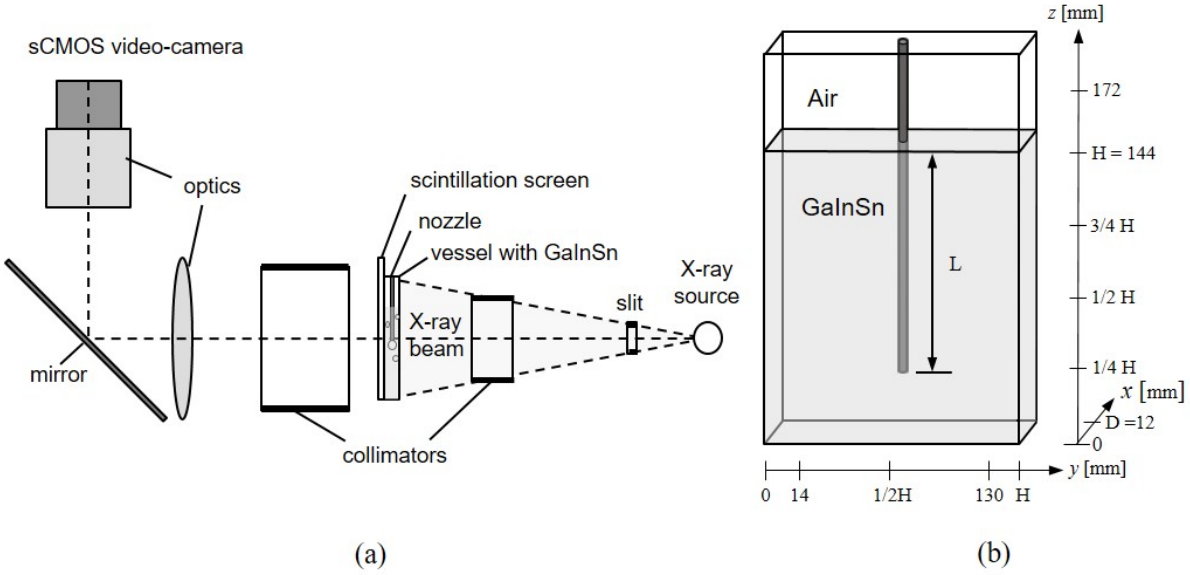

Fig. 1 - Schematic drawings of (a) the experimental setup and (b) the vessel and positions of the top submerged lance.

B. *Techniques of Image Processing*

This section contains a brief description of the various techniques for image processing. All of the methods applied in this study were implemented in Python 3.7.2 using various open source programming libraries. The specific steps of image processing based on the procedures described below are exemplified by detail views of a single bubble in Figure 2. The first step is to rescale the gray values of the raw images. These are originally stored as 16bit values which are not supported by most image processing functions. In addition, the chosen camera settings lead to maximum intensity values much smaller than 2^{16}. Therefore, the intensity range is rescaled into 8bit values linearly without compromising the image contrast:

$$[I_{GaInSn} \ldots I_{Ar}] \rightarrow [0 \ldots 2^8] \tag{1}$$

where I_{GaInSn} and I_{Ar} are the 16bit reference intensities of the image for a fluid container completely filled with liquid metal or Argon, respectively. The resulting 8bit grayscale images are denoted as rescaled image from now (*cf.* Figure 2(a)).

In order to reduce the image noise, a bilateral Gaussian blurring [19] is applied to the rescaled image. This nonlinear filter effectively reduces the noise in a wide frequency range without obliterating sharp edges like the gas-liquid phase boundaries as shown in Figure 2(b). An accordingly rescaled and smoothed background image which is recorded without gas injection is subtracted from the smoothed images. This reduces the inhomogeneous intensity distribution caused by the presences of the submerged lance and the spatial Gaussian intensity distribution of the X-ray beam.

As a next step, an adaptive threshold [20] is applied to separate the individual bubbles and bubble clusters from the background as shown in Figure 2(c). Due to the non-uniform distribution (Gaussian shape) of the

X-ray beam in the *y*-*z* plane, bubbles located close to the side walls are less illuminated than bubbles located in the centre. Although the background subtraction described above mitigates this, a global threshold value would either ignore or underestimate less illuminated bubbles near the wall or overestimate large bubbles in the centre. An adaptive threshold method offers a solution of this problem by computing a different threshold value for each pixel as a Gaussian weighted mean value of the local neighbourhood. This provides an increased robustness and higher sensitivity of bubble detection. The only significant drawback of adaptive thresholding is the occurrence of locally frayed edges of the detected bubbles which can be seen in Figure 2(c). This is compensated by a succession of an erosion and a dilation filter also known as the morphological opening filter [21] which yields a physically reasonable, smooth phase boundary as shown in Figure 2(d). To enable further statistical analysis, the binary images are labelled. Hereby each region of connected pixels belonging to a certain bubble is assigned a specific number. Quantities as the projected area can now be determined for each bubble individually.

C. *Computation of the local void fraction*

The local void fraction $\alpha(y, z)$, which can be assigned to a specific pixel, is associated with the extension of the bubble along the *x*-direction being the direction of X-ray transmission. The local X-ray intensity is given by the Beer-Lambert law that relates the attenuation of the X-ray beam to the properties of the material which is penetrated by the beam. The Beer-Lambert law is described as

$$I = I_0 e^{-\mu x} \tag{2}$$

where I_0 is the primary beam intensity, μ is the X-ray absorption coefficient of the absorbing material and x is the coordinate along the X-ray beam. In the present study, the reference intensity of Argon is regarded as the primary beam intensity because the gas hardly attenuates the X-ray beam compared to the liquid metal in the fluid layer. This corresponds to the assumption $\mu_{GaInSn} \gg \mu_{Ar} \approx 0$. The absorption coefficient of the liquid metal μ_{GaInSn} is estimated by the reference intensities of I_{GaInSn} and I_{Ar} and the thickness of the layer D (assuming a monochromatic X-ray beam):

$$\mu_{GaInSn} = \frac{1}{D} \cdot \ln \frac{I_{GaInSn}}{I_{Ar}} \tag{3}$$

In case of the bubbly flow the local X-ray intensity $I(y, z)$ is given by

$$I(y,z) = {I_{Ar}}^{-\mu_{GaInSn}(D - L(y,z))} \tag{4}$$

where $L(y, z)$ is the thickness of the gas bubble. By converting eq. (4) this value can be calculated as follows

$$L(y,z) = \frac{\ln \frac{I(y,z)}{I_{Ar}} + \mu_{GaInSn} \cdot D}{\mu_{GaInSn}} \tag{5}$$

The local void fraction $\alpha(y, z)$ is defined as

$$\alpha(y,z) = L(y,z)/D \tag{6}$$

Now, the volume V_{B_i} for a particular bubble can be calculated by integrating for $\alpha(y, z)$ each individual bubble area A_i:

$$V_{B_i} = D \int_{A_i} \alpha(y,z)\, dA, \tag{7}$$

where A_i is determined from the labelled binary image after the morphological transformation (see Figure 2(d)). Figure 2(e) shows a bubble image in which the colours reflect the bubble thickness in the beam direction. In order to only regard the pixel areas for which the presence of a gas bubble was detected, the original raw images were masked by the binary images after the morphological transformation.

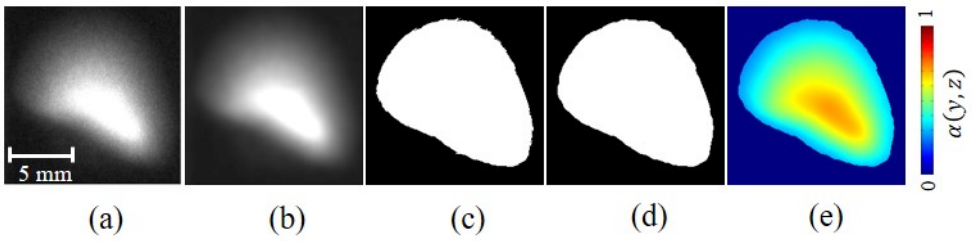

Fig. 2 - Consecutive steps of image processing leading to (a) a rescaled gray-scale image, (b) a bilaterally blurred image, (c) a binary image resulting from the adaptive thresholding, (d) a binary image after morphological transformation and, (e) a two-dimensional distribution of the local void fraction inside the bubble projection area.

Figure 3 exemplary shows some representative images obtained by image processing. Figure 3(a) presents a rescaled image for a gas flow rate of Q_{gas} = 0.05 l/s and the bottom injection position. In this particular image the intensity values are logarithmically rescaled to enhance the visibility. Figure 3(b) and 3(c) show the binary image after morphological transformation and the two-dimensional distribution of the local void fraction, respectively. Both images are calculated from the rescaled image in Figure 3(a). Figure 3(d) shows a color representation of the temporal average of a sequence of one second of the respective binary images. The resulting data can be interpreted as the probability $P(y, z)$ to detect a gas bubble at a certain location during the averaging period. Moreover, it can also be considered as a rough estimation of the time-averaged void fraction. Figure 3(d) reveals the dynamics of the bubble trajectories: note the splitting of the main path of the rising bubbles beneath the free surface. Moreover, the trajectories of the smaller bubbles become visible. As a comparison, Figure 3(e) shows the time-averaged local void fraction for the same averaging period as chosen in Figure 3(d). While Figure 3(d) possesses a higher contrast, which allows for a better monitoring of small bubbles, Figure 3(e) is more accurate in terms of quantitative values of the local void fraction.

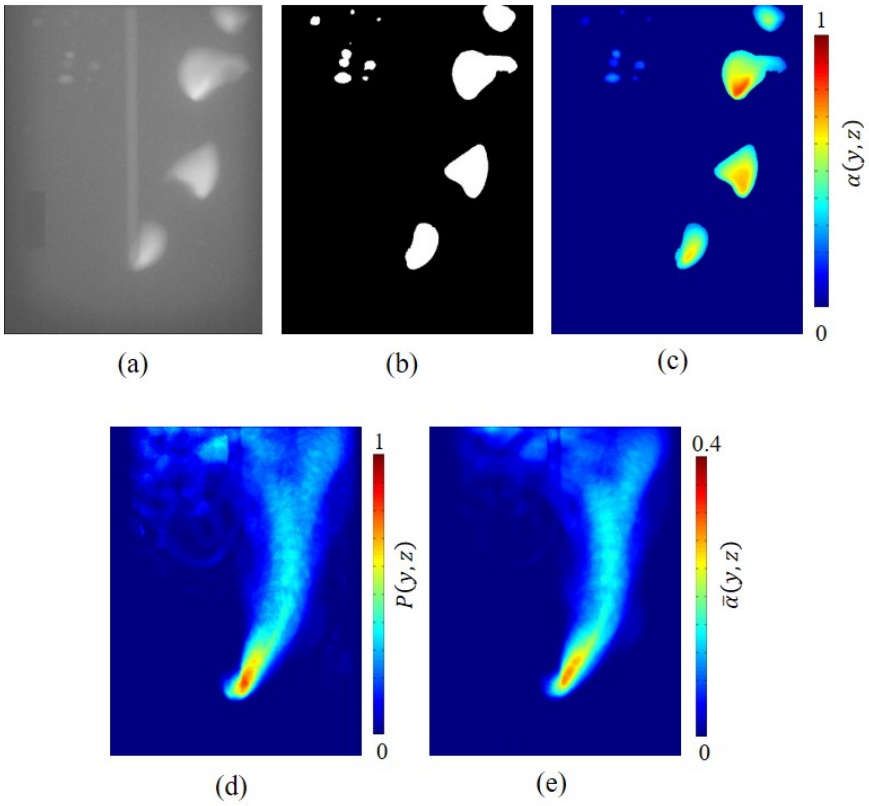

Fig. 3 - Distribution of the gas phase in the fluid vessel for a gas flow rate of Q_{gas} = 0.05 l/s and the bottom injection position (L = 3/4 H): (a) rescaled gray-scale image, (b) binary image, (c) two-dimensional distribution of the local void fraction, (d) the probability of bubble presence $P(y, z)$ for an averaging period of one second, and (e) distribution of the time-averaged local void fraction for the same averaging period.

III. Results

A. *Qualitative characterization of the bubbly flow*

Figure 4 contains exemplary rescaled raw images of the bubbly flow recorded at a gas flow rate of Q_{gas} = 0.05 l/s for three different submergence depths. Corresponding movie sequences are available as electronic supplementaly material. [S1-S3] The image sequence in Figure 4(a)-(c) shows the formation, the rise and the burst of a single bubble at the free surface for the case of a submergence depth of L = 1/4 H (top). The projection area of the bubble, which at no time takes a circular or an elliptical shape, reaches a lateral extent up to about 20 mm. The shape of the bubble is not stable, but shows significant oscillations. Due to the impact of the bubbles, the free surface is strongly deflected. Occasionally, one can observe the splashing of single droplets.

The images recorded for a submergence depth of L = 1/2 H (middle) (Figure 4(d)-(f)) usually show two or three large bubbles within one frame. Successive bubbles approach each other after detachment from the lance tip and bubble collisions occur. In detail, the succeeding bubble is sucked into the wake of the prevenient bubbles, and therefore, both bubbles are strongly deformed. However, hardly any coalescence is observed. Apparently, the bubble contact time is too short before the bubbles reach the free surface. After a certain time following the onset of gas injection, it becomes apparent that the bubbles preferably rise on one side next to the lance, which is a clear indication of the formation of a pronounced recirculation flow in the liquid bath.

Figure 4(g)-(i) represent the flow structure in the case of a submerged depth of L = 3/4 H (bottom). The lateral deflection of the bubble trajectories reveals the occurrence of a distinct asymmetric large-scale circulation in the liquid metal. The bubbles interact very strongly with each other. Usually, bubble clusters occur below the surface and coalescence can be observed there. In the example shown here, the bubbles come up against the free surface at a position to the right of the lance resulting in a strong bulge of the free

surface. Especially in this area, larger bubbles disintegrate into smaller bubbles. The majority of the bubbles are released at the free surface, but a remarkable number of small bubbles are captured by the large-scale circulation and transported into deeper zones of the fluid. On the left side of the lance, a strong depression of the free surface can be observed in combination with gas entrainment which also creates a remarkable number of small bubbles. The small bubbles remain trapped in the recirculation vortex for a long time. Seemingly, the predominant part of the small bubbles results from the gas entrainment at the free surface. A frequent breakup of the large ascending bubbles into smaller ones before approaching the free surface is hardly observed. [S3]

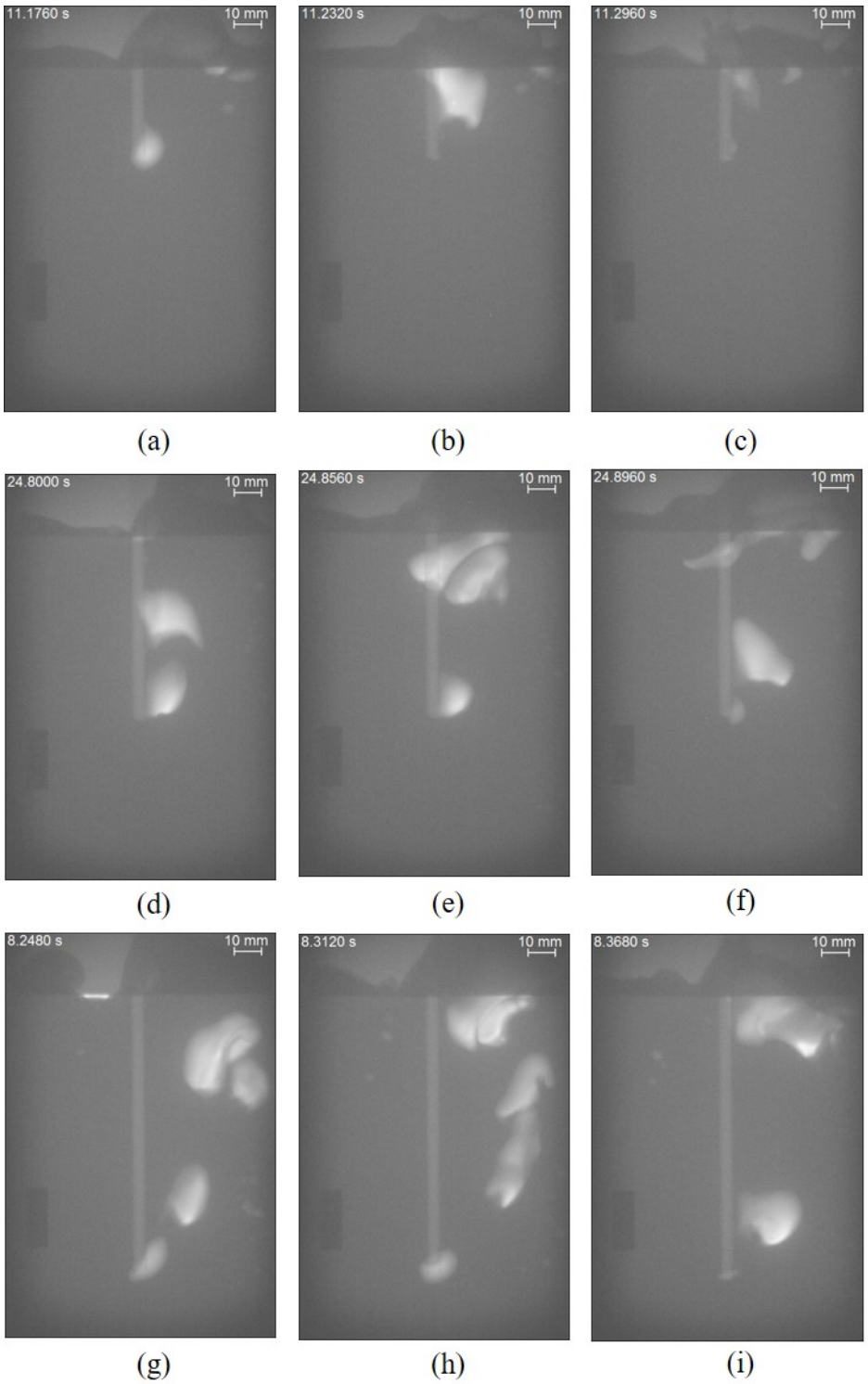

Fig. 4 – Sequences of rescaled images for a gas flow rate of Q_{gas} = 0.05 l/s for different submerged depths of the lance: (a)-(c) L = 1/4 H (top), (d)-(f) L = 1/2 H (middle), and (g)-(i) L = 3/4 H (bottom).

Figure 5 presents contour plots of the probability of bubble presence at a certain location $P(y,z)$ for different points in time calculated for an averaging period of one second. Figure 5(a)-(c) display the probability distributions for a gas flow rate of Q_{gas} = 0.05 l/s. Immediately after starting the gas injection (see Figure 5(a)), a straight rise of the bubbles can be observed. However, only a few seconds later (*cf.* Figure 5(b)) the trajectories of the bubbles quickly change due to the onset of a strong large-scale circulation in the fluid. The form of the mean bubble path reveals the asymmetric structure of the large-scale recirculation. The transition from the originally symmetrical to the asymmetrical flow pattern might be caused by instabilities arising from the asymmetric bubble wake, fluctuations of the free-surface or wall effects leading to a horizontal non-homogeneity in the force balance. This transition of the flow structure is also observed in the case of bubble chains generated by bottom gas injection. [22–25] The bubbles prefer to follow the trace of the preceding bubbles. This behavior reduces the hydrodynamic drag force acting on the bubbles and enhances the bubble rising velocity. The asymmetric flow pattern is also observed half a minute after switching on the gas flow (Figure 5(c)) and is maintained throughout the entire measurement time. Figure 5(b) and (c) also render the phenomenon of gas entrainment at the free surface visible. This feature becomes especially pronounced for the case of the lance bottom position. Furthermore, it is observed that while approaching the free surface, the bubbles make a sideways motion and breakup occurs just below the free surface. The small bubbles that are then captured by the recirculation and transported downward are either the breakup products of these larger bubbles or form directly on the free surface.

The bubble trajectories are subject to distinct fluctuations, which may also be strong enough to change the direction of the bubble path (right or left of the lance). Such a reciprocating motion of the trajectories occurs primarily in the case of large gas flow rates and small immersion depths of the lance. The deeper the lance is immersed, the more intense and stable the recirculating flow becomes. For instance, for the deepest immersion depth of the lance and all gas flow rates considered here the time-averaged shape of the mean bubble path is almost kept constant throughout the entire measurement. In contrast, the likelihood of the bubbles rising to the right or left of the lance is nearly balanced for the upper and middle lance position at a sufficiently high gas flow rate. As an example, Figure 5(d)-(f) contain probability distributions for a gas flow rate of Q_{gas} = 0.1 l/s injected at the middle lance position. While the flow pattern appears to be symmetric just after the beginning of the experiment (see Figure 5(d)), the transition to the asymmetrical flow pattern happens quickly. Here, the bubble trajectories are initially curved to the right (see Figure 5(e)) before the bubbles move into the left side of the container (see Figure 5(f)). The trajectories change their orientation around 20 s after the onset of gas injection and maintain this direction until the end of the measurement.

The characterization of the gas distribution is complemented by a long-term average covering the entire measurement (≈ 40 s) of the probability of bubble presence shown in Figure 6. Figure 6(a)-(c) show time-averaged gas distributions for a volumetric flow rate of Q_{gas} = 0.05 l/s and the three different lance submergence depths. At this gas flow rate, an asymmetric bubble path is observed for all three injection positions. A change in the direction of bubble rise is not observed here. Figure 6(d) presents the situation of the higher gas flow rate (Q_{gas} = 0.1 l/s) corresponding to the experiment already shown in Figure 5(d)-(f). Due to the observed spontaneous change in direction of the bubble path after approximately half of the measuring time, the result for the total measuring time is a nearly symmetric gas distribution. It has to be noticed, however, that the maximum measuring time within this study is only 40 s. Therefore, the data do not allow out for any prediction with regard to the flow stability during longer time intervals.

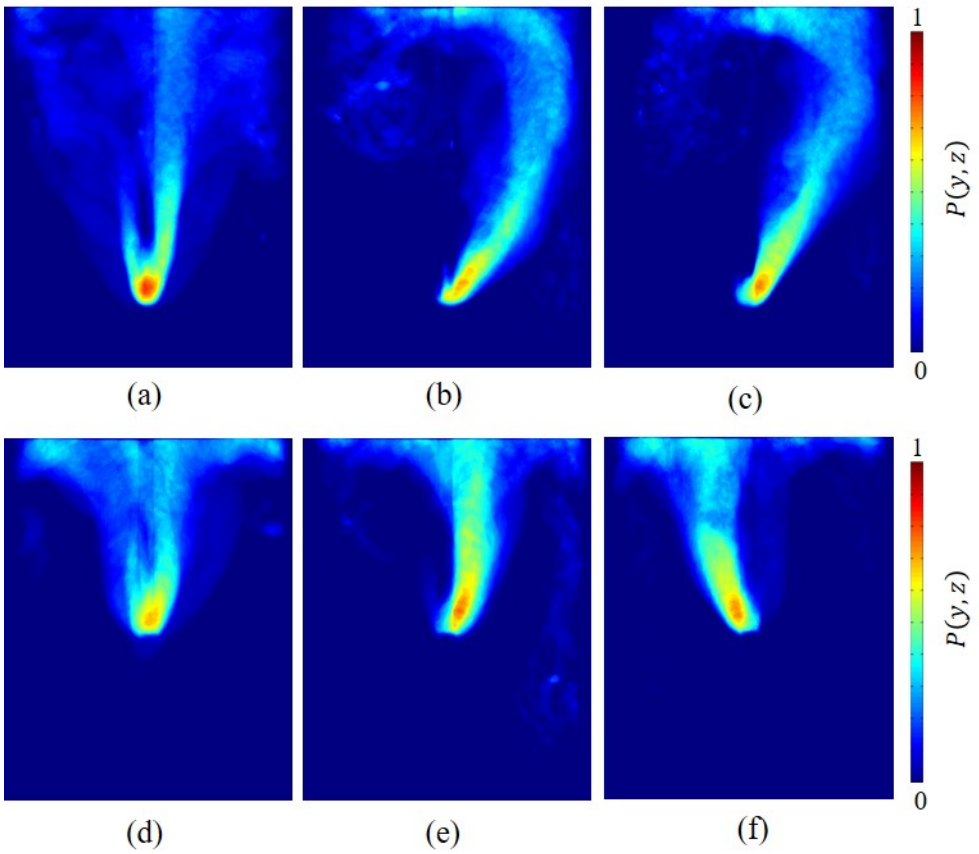

Fig. 5 - Probability to detect a gas bubble (averaging period: 1 s) for a gas flow rate of Q_{gas} = 0.05 l/s and the bottom injection position (L = 3/4 H) at different points in time after onset of gas injection: (a) 1 s, (b) 4 s, and (c) 31 s, and for a gas flow rate of Q_{gas} = 0.1 l/s and the middle injection position (L = 1/2 H):(d) 1 s, (e) 4 s, and (f) 31 s.

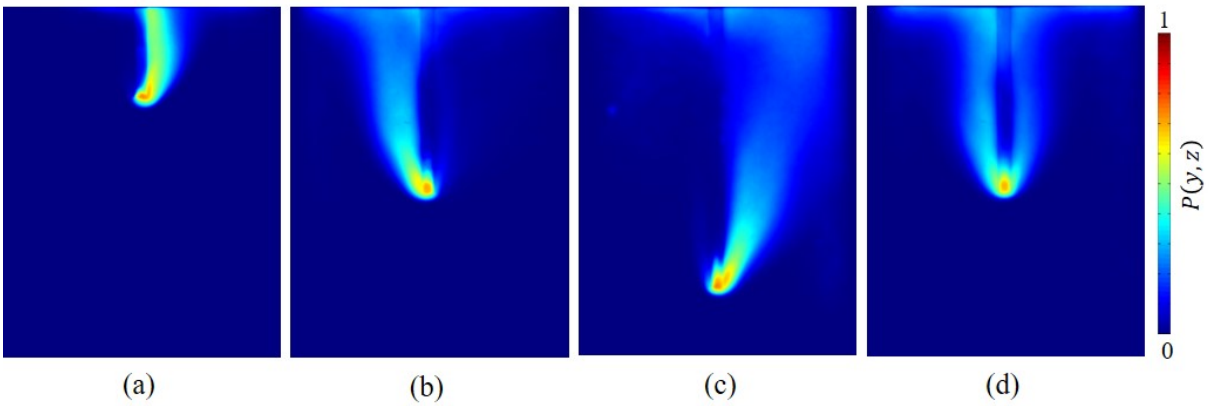

Fig. 6 - Probability of bubble presence during a measurement time of 40 s for a gas flow rate of Q_{gas} = 0.05 l/s at three different lance submergence depths: (a) L = 1/4 H (top), (b) L = 1/2 H (middle), and (c) L = 3/4 H (bottom), and (d) for a gas flow rate of Q_{gas} = 0.1 l/s at L = 1/2 H (middle).

B. *Frequency of bubble injection*

For determining the frequency of bubble injection temporal changes of the image intensities were evaluated along one horizontal measuring line which, strictly speaking, is a thin stripe with an extension of 1.5 mm in z-direction. This measurement line is set at a height of 20 mm above the injection position as illustrated in

Figure 7(a). The time-dependent integral S (t) of the intensities within this stripe is calculated for each time step as

$$S(t) = \int_{z=H-L+20}^{z=H-L+21.5} \int_{y=14}^{y=130} I_{(y,z)}\, dy\, dz \tag{8}$$

The configuration and the corresponding coordinate system are shown in Figure 7(a). Exemplary results obtained at the bottom injection position for a gas flow rate of Q_{gas} = 0.05 l/s are depicted in Figure 7(b). Local maxima of the intensities occur if a single bubble crosses the measuring line. Typical frequencies of bubble injections are obtained by the Fast Fourier Transformation (FFT, see Figure 7(c)) of the temporal signal. Smoothing of the spectra obtained by FFT is achieved by dividing the time series of the data into time intervals of 8 s. A Gaussian fitting is applied to the smoothed spectrum. The center frequency of the obtained Gaussian function is taken as the bubble injection frequency.

Figure 8 shows the results for the bubble injection frequency as a function of the gas flow rate. For the gas flow rates considered here the analysis yields bubble frequencies in a range between 10 and 13 Hz. In case of the top and middle lance position, the frequencies decrease slightly with increasing gas flow rate, while the gas volumetric flow rate does not have a significant effect on the bubble detachment frequency for the bottom injection position. By averaging the bubble frequencies for a given lance position across all gas flow rates studied here, the following mean values are obtained: f_{top} = 11.40 ± 1.44 Hz (top), f_{middle} = 12.52 ± 0.76 Hz (middle) and f_{bottom} =13.17± 0.25 Hz (bottom). The fluctuation range around the mean value decreases the deeper the lance is immersed.

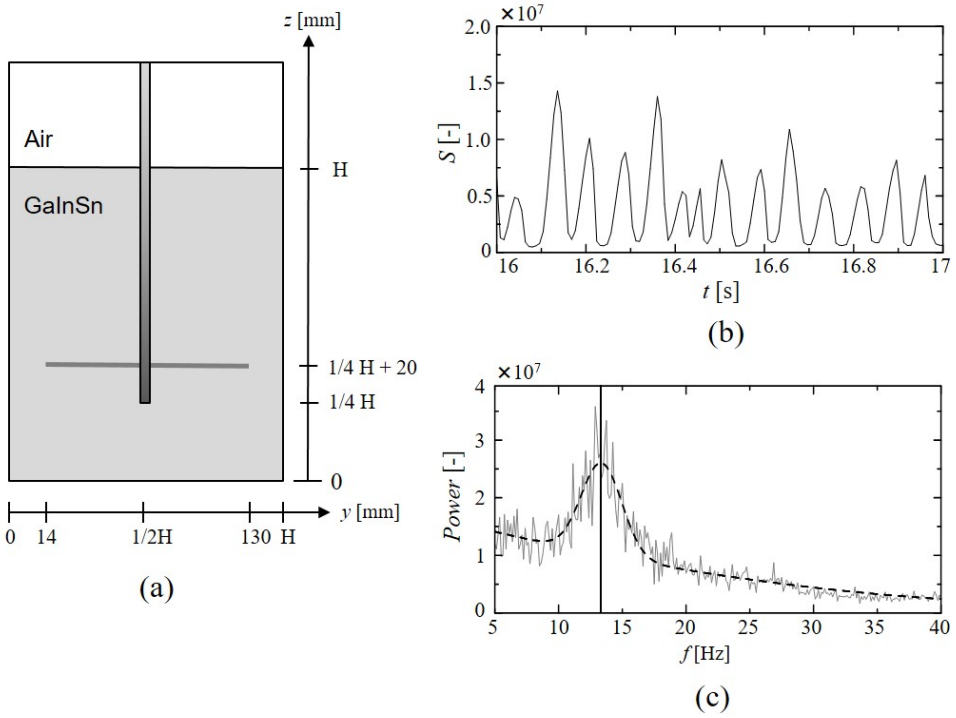

Fig. 7 - (a) Arrangement of the measurement line in the fluid layer, and (b) detail of the time series of the sum of intensities S (t) along the measurement line at z = 20 mm for a gas flow rate of Q_{gas} = 0.05 l/s at the bottom injection position (L = 3/4 H) and (c) corresponding power spectrum of S (t) (the dashed line indicates the Gaussian fit and the solid line indicates the bubble injection frequency).

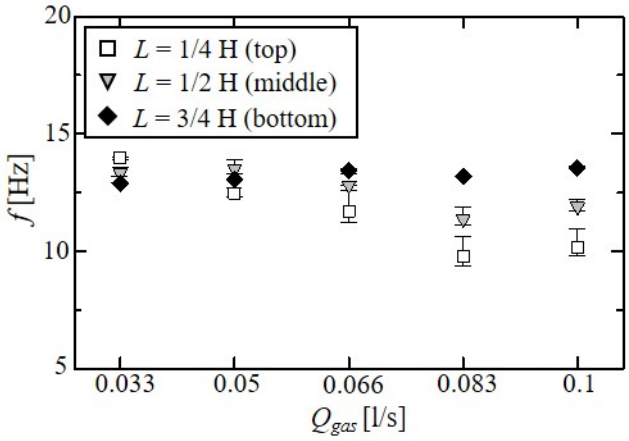

Fig. 8 - Bubble injection frequency as a function of the gas flow rate Q_{gas} at three different injection positions.

C. *Bubble sizes and bubble distributions*

With regard to the almost constant or even partially decreasing bubble detachment frequency with increasing gas flow rate, increasing bubble sizes are to be expected. In this study, the bubble size is estimated in two different ways. First, the mean bubble volume V_f can be calculated from the chosen gas flow rate Q_{gas} and the mean frequency of bubble injection f

$$V_f = \pi d_f^3/6 = Q_{\text{gas}}/f \tag{9}$$

Thus, the equivalent diameter of an equivalent spherical bubble, d_f, is given as follow

$$d_f = \sqrt[3]{\frac{6Q_{gas}}{\pi f}} \tag{10}$$

The resulting values of $d_f(Q_{\text{gas}})$ for the case of the bottom injection position are included in Figure 11.

Second, the bubble size can be estimated by determining the two-dimensional projection area of the bubble in the binary image obtained through image processing as explained in section II.B. In most previous studies [6,13,14,24,25] this method was used to estimate the bubble size. Assuming a spherical bubble the diameter d_A is calculated from the bubble area A

$$d_A = \sqrt{\frac{4A}{\pi}} \tag{11}$$

Finally, another option is provided on the basis of the local void fraction calculated from the X-ray images as explained in section II.C. This method offers a three-dimensional reconstruction of individual bubbles, thus allowing for an accurate determination of the individual equivalent bubble diameter d_V calculated as:

$$d_V = \sqrt[3]{\frac{6V_B}{\pi}} \tag{12}$$

where the bubble volume V_B is given by eq. (7).

Fig. 9 contains exemplary snapshots of the two-dimensional distribution of the local void fraction $\alpha(y,z)$ for three different gas flow rates at the bottom injection position. In general, three or four larger bubbles are observed at one frame, which separate from the nozzle and rise to the free surface. In addition, the smaller bubbles are again visible here, which form due to bubble breakage or gas entrainment at the free surface

and are conveyed with the recirculating flow. Obviously, both the projected bubble area and the thickness of the gas layer within the corresponding projected bubble area become larger with increasing gas flow rate. The latter is reflected in the higher values of the local void fraction $\alpha(y,z)$. In case of the highest gas flow rate condition at of Q_{gas} = 0.1 l/s, the void fraction approaches values close to unity for the most part of the bubble. However, from the movies [S4] it becomes clear that there is still a liquid film between the gas bubble and the side wall, which allows a continuous movement of the bubbles. In addition to this, an increasing number of small bubbles are observed for the higher gas flow rates.

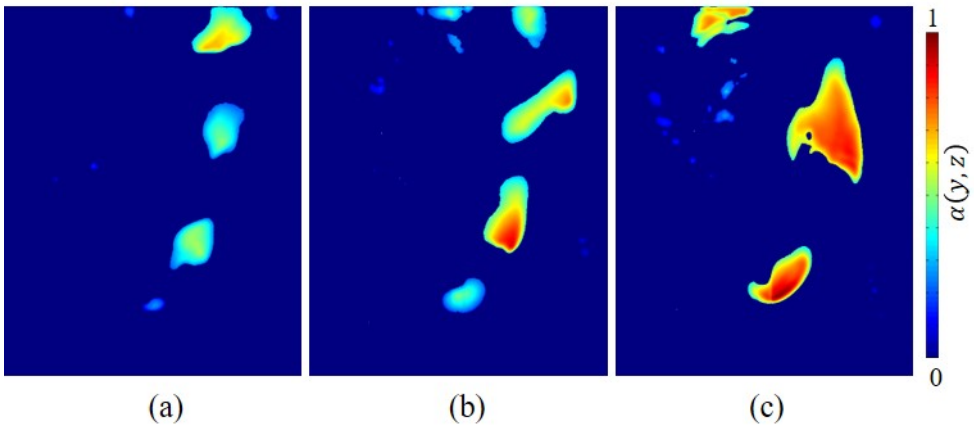

Fig. 9 - Snapshots of the two-dimensional distribution of the local void fraction for different gas flow rates: (a) Q_{gas} = 0.033 l/s, (b) Q_{gas} = 0.066 l/s and (c) Q_{gas} = 0.1 l/s at the bottom injection position (L = 3/4 H).

Figure 10 depicts representative histograms showing the average number of bubbles per frame $\overline{N}$ for varying equivalent diameters d_A and d_V, respectively (see eqs. (10)-(12)). The histograms shown here for the case of the bottom injection position involve 3500 frames and cover a period from 2s to 30s after starting the gas injection. The following values are obtained for the total number of bubbles per frame (sum over all $\overline{N}$): 7.70 (Q_{gas} = 0.033 l/s), 14.50 (Q_{gas} = 0.066 l/s) and 19.13 (Q_{gas} = 0.1 l/s). These values confirm the main tendency, which is also evident in Figure 9 that the number of bubbles increases significantly with growing Q_{gas}. It is noticeable that there is a substantial increase in the number of small gas bubbles with increasing gas flow rate. For the two higher gas flow rates (*cf.* Figure 10(c)-(f)) the bubble size distribution becomes almost bipolar with the small bubbles dominating in numbers. It appears to be reasonable to assume that the two peaks in the bubble size distribution are associated with primary bubble generated directly by the gas injection and secondary bubbles arising bubble breakup or the gas entrainment at the free surface.

As a next step, the mean equivalent bubble size of the primary bubbles rising from the tip of the lance towards the free surface was determined. For this analysis, the smaller bubbles were excluded and only the bubbles with a diameter greater than a threshold value, which was determined as the minimum between the peaks associated with the primary and secondary bubbles, respectively, were included in the calculations. The respective threshold values are marked as dashed lines in Figure 10. The calculations are based on the evaluation of about 9000 bubbles per data point. The results are compared in Figure 11 with the equivalent diameter d_f obtained from eq. (10) based on the bubble detachment frequency f and the gas flow rate Q_{gas}. The values for $\overline{d_V}$ are shown for the bottom and the middle injection position. The results at the top injection position are not included in Figure 11 because in this situation the bubble is always strongly affected by either the detachment at the nozzle or the interaction with the free surface.

The resulting values $\overline{d_A}$ are slightly overestimated compared to the values of d_f. This is not surprising since the real void fraction (gas distribution) associated with the bubble projection area is not taken into account by the binary images. In contrast to this, the values obtained for $\overline{d_V}$ are found to be remarkably smaller than the values of d_f. It is possible that the allocation of the two peaks in the bubble size distribution to primary and secondary bubbles does not prove accurate enough. Bubble breakup often occurs during rising and the bubbles usually do not fragment into nearly equal sized bubbles. [S3, S4] Often only one or two smaller bubbles separate, which only slightly changes the size of the original bubble. These larger products of the

bubble breakup also contribute to the peak of the primary bubbles in Figure 10 and are thus erroneously taken into account for the calculation of the average value $\overline{d_V}$ which at the end is then calculated as being too low. The bubble size results, regardless of the calculation method, show the same trend of increasing the bubble diameter with the gas flow rate as shown in Figure 11.

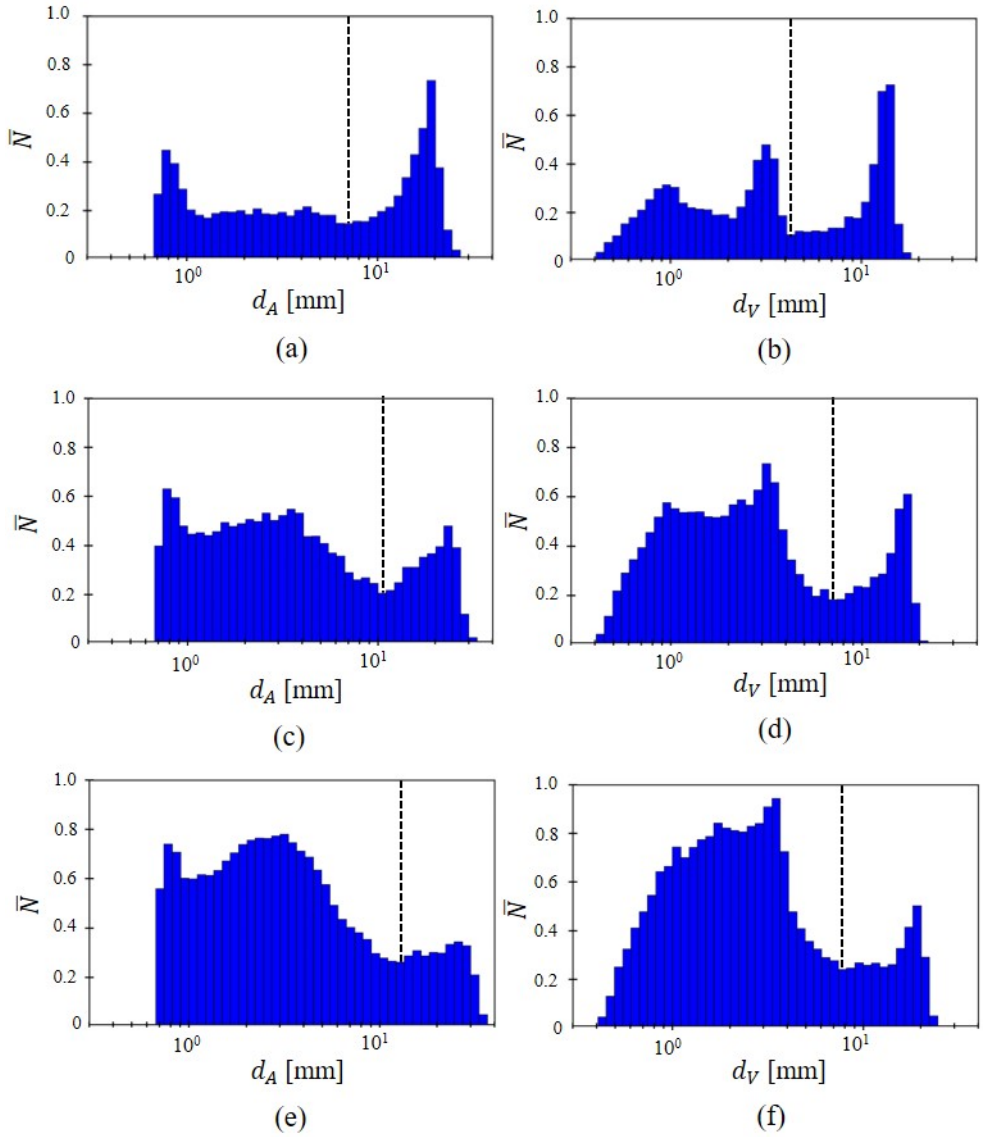

Fig. – 10 Histograms of the average numbers of bubbles per frame for varying equivalent bubble diameters estimated by the projected area d_A and by the bubble volume d_V for different gas flow rates: (a-b) Q_{gas} = 0.033 l/s, (c-d) Q_{gas} = 0.066 l/s and (e-f) Q_{gas} = 0.1 l/s. All histograms show the data obtained for the bottom injection position (L = 3/4 H). The dashed line represents the threshold chosen for the minimum in the bubble size distributions.

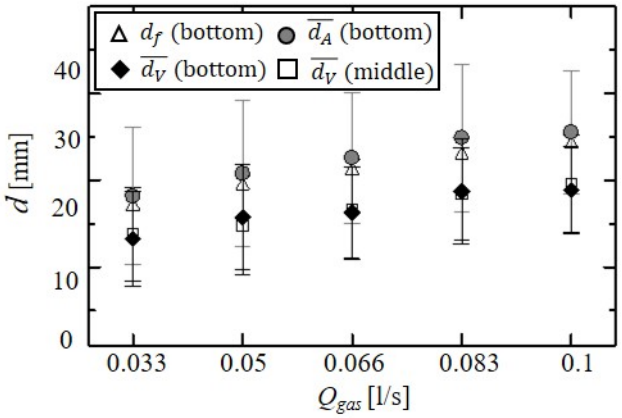

Fig. – 11 Mean equivalent bubble diameter as a function of the gas flow rate Q_{gas} for the bottom injection position.

IV. Discussion

The visualization of the liquid metal bubbly flow created by gas injection through a top submerged lance reveals complex pattern which are distinctly influenced from both the gas flow rate and the lance immersion depth. The flow dynamics involve phenomena of bubbly interaction such as collision, coalescence and breakup as well as the entrainment of small bubbles at the free surface and their transport by a strong liquid flow into deeper liquid domains. The parameter range in this study is restricted to low and moderate gas flow rates. This means that there was no formation of a gas jet at the nozzle during gas injection at any time. Thus, all experiments are conducted in the bubbling mode, in which the bubbles separate individually from the nozzle. The bubble detachment frequency f is essentially governed by the discharge velocity of the gas into the liquid. The mean gas velocity in the lance u_{gas} is calculated by the gas flow rate Q_{gas} and the inner lance diameter d_{in}

$$u_{gas} = Q_{gas}/\pi(d_{in}/2)^2 \tag{13}$$

Leibson *et al.* [27] studied bubbly flows in air-water systems by bottom gas injection and suggested the lance Reynolds number

$$Re_l = u_{gas} d_{in}/\nu_g \tag{14}$$

as the related non-dimensional parameter for determining the gas injection regime (with ν_g as the kinematic viscosity of the gas phase). The transition between the bubbling regime and the jetting regime was reported for $Re_l \approx 2\times10^5$. In our study we obtain lance *Re* numbers between 700 and 2120 for gas flow rates of 0.033 l/s and 0.1 l/s, respectively. Gosset *et al.* [6] measured the bubble detachment frequency for the configuration of the top submerged lance in air-water for different lance diameters and gas flow rates. In case of a lance diameter of 9 mm the frequency remains constant for low gas flow rates up to about 1.5 l/s rises sharply before reaching a maximum value at 3.5 l/s. At higher gas flows f decreases, but remains above the values for small gas flows. In our study we found a nearly constant bubble frequency at the bottom lance position within the range of gas flow rates investigated. Because only rather low gas flow rates are considered here, this behavior agrees very well with the plateau reported by Gosset *et al.*[6] for Q_{gas} < 3.5 l/s (Re_l < 2670). Although the gas flow rates investigated in our study are, at first sight, much smaller than in Gosset *et al.*[6], comparable values are achieved for u_{gas} and Re_l due to the smaller lance diameter (see table 1).

Table 1 – Comparison of experimental parameters Q_{gas}, u_{gas} and Re_l considered in [6] and in the present work.

	Q_{gas} [l/s]	u_{gas} [m/s]	Re_l
Gosset et al.[6] (d_{in} = 9 mm)	0.05 … 5	0.785 … 7.85	382 … 3820
this study (d_{in} = 5 mm)	0.033 … 0.1	1.68 … 5.09	700 … 2120

The reported frequencies of bubble injection in water [6] are about half of the frequencies obtained in liquid metal. This discrepancy could be related to the distinct differences in buoyancy, surface tension and the wetting behaviour at the injection nozzle.

Gosset *et al.*[6] proposed a dimensionless correlation for the prediction of the bubble injection frequency in terms of the Strouhal number and the ratio of Weber number and Bond number. Here, the injection Strouhal number is defined by the bubble injection frequency *f*, the gas velocity u_{gas} and the inner lance diameter d_{in}.

$$St = \frac{f d_{in}}{u_{gas}} \tag{15}$$

The process of bubble formation at the tip of the lance is determined by a force balance between the inertia of the injected gas, buoyancy and surface tension. The Weber number indicates the ratio between the inertial force and the surface tension. In contrast to [6] we use the inner diameter of the lance as a characteristics length for calculating the inertia of the gas discharging from the nozzle:

$$We = \frac{\rho_{gas} d_{in} u_{gas}^2}{\sigma} \tag{16}$$

where σ denotes the surface tension of the liquid metal. The Bond number is the ratio of the buoyancy (ρ_l is the fluid density) acting on the forming bubble with diameter d_f to the surface tension.

$$Bo = \frac{(\rho_l - \rho_{gas}) g {d_f}^2}{\sigma} \tag{17}$$

Thus, the ratio of Weber number and Bond number corresponds to the ratio of the inertia and buoyancy.

$$\frac{We}{Bo} = \frac{d_{in} u_{gas}^2}{(\rho_l/\rho_{gas} - 1) g d_f^2} \tag{18}$$

The corresponding results for the liquid metal experiments performed in this study are shown in Figure 12. Here, the analysis is restricted to the bottom lance position. At a position closer to the free surface, an influence of the intense fluid flow at the free surface on the detachment of the bubbles cannot be fully excluded. Such an interaction is difficult to describe in a quantitative way, which is why we did not consider the other two lance positions here. A power law fit indicated as a dotted line in Figure 12 suggests a scaling of

$$St = 0.00047 \left(\frac{We}{Bo}\right)^{-0.70 \pm 0.02} \tag{19}$$

where the exponent is calculated by a least square approximation. In comparison, slightly different values were reported for the exponent (0.61) and the coefficient (0.00126) in the water experiments by Gosset *et al.* [6] Based on the available data, it is not possible to definitively clarify what justifies this deviation. Both experiments differ in several features regarding the properties of the liquids or the geometry of the fluid vessel. The fluid properties, namely the strong mismatch in surface tension, are taken into account by the dimensional analysis presented above. The question, of whether the difference in geometry or other uncertainties can explain the deviations in the power law fit, needs to be addressed in future studies.

Moreover, the examined parameter range is smaller in the present study ($0.0019 < We/Bo < 0.009$) compared to [6]($10^{-6} < We/Bo < 1$). Therefore, further studies will consider an extension of the experimental parameter range.

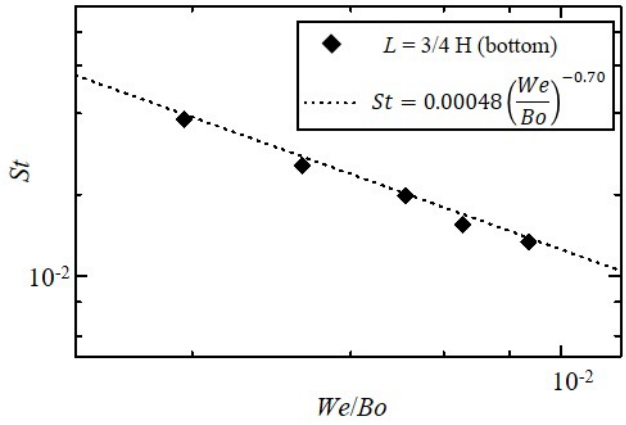

Fig. 12 – Variation of the injection Strouhal number as a function of the ratio of the Weber number to the Bond number (the dotted line represents the fit $St = 0.00048 \times (We/Bo)^{-0.70}$).

It is widely accepted, that a motion of the liquid bath can promote the detachment of the bubbles and result in a higher bubble frequency. Goda *et al.* [7] investigated the effect of a cross-flow on the frequency of bubble formation by rotating the fluid vessel. The authors reported that the bubble frequency can increase by a factor of up to three due to the swirling motion of the fluid. In the flat vessel used in the present study the transition from the originally symmetric to an asymmetric bubble path occurs after a certain time. Liu *et al.*[25] reported a similar behavior of bubble chains generated by bottom injection in a liquid metal by both numerical simulation and experiments. The transition from the symmetrical to the asymmetrical flow pattern is associated with the occurrence of an intense fluid flow in the vessel. The bubble-induced liquid motion becomes stronger the deeper the lance is immersed in the bath. This might explain the differences between the bubble frequencies found for the various lance positions (compare Fig. 8). However, at this point we still have no conclusive explanation for the decline of the frequency with increasing gas flow rate at higher lance positions. Further investigations of the flow structure in the liquid bath–are considered necessary in order to achieve a better understanding of this phenomena.

Our experiments clearly indicate, that, in particular at the high gas flow rates, the bubble shape is strongly influenced by the restricted dimension of the container in *x*-direction (parallel to the X-ray beam). At a gas flow rate of 0.1 l/s, the bubbles extend over almost the entire thickness of the container for nearly their complete bubble projection area. However, a dewetting of the container wall does not occur. There is still a thin liquid film between the bubble and the wall which keeps the bubble as a free moving object. Although the bubble does not stick to the wall, its movement is largely determined by the friction in the near viscous boundary layers.

A large number of smaller bubbles are produced at high gas flow rates due to bubble breakup and gas entrainment at the free surface. The number of small bubbles in the volume is then also increased by the fact that they are captured by the intense recirculating flow in the container which in our experiment reaches the maximum intensity with the bottom lance position. This, taken together, provides for a significant increase in the specific phase boundary between gaseous and liquid. With regard to the TSL process, this would be equivalent to achieving a high chemical reaction rate.

V. Conclusions

Complex bubbly flows arising from gas injection through a top submerged lance (TSL) were investigated by laboratory experiments in a narrow enclosure filled with liquid metal. The experiments were carried out in GaInSn, a ternary alloy that is liquid at room temperature. The dynamics of the bubble motion were

visualized by means of X-ray radiography combined with high-speed imaging. The findings of this study can be summarized as follows:

- The X-ray radiography was demonstrated as an effective method for providing essential information concerning the structure of gas-liquid two-phase flows in non-transparent fluids such as metallic melts. It allows for a qualitative description of the flow regimes as well as for quantification of the bubbles properties or the local void fraction. By considering the local attenuation coefficients, even the three-dimensional bubble dimensions can be reconstructed which is the basis for estimating the volume of each individual bubble.

- The rising gas bubbles drive a recirculating flow in the liquid whose intensity increases with increasing gas flow rate. Although the bubble trajectories are subject to fluctuations, the flow structure stabilizes with increasing immersion depth of the lance. In particular, in case of the bottom lance position a persistent lateral deflection of the bubble trajectories indicates the formation of a distinct asymmetric large-scale circulation in the liquid metal. In contrast, the lower the depth of immersion, the greater is the likelihood that the bubbles will rise evenly distributed on both sides of the lance.

- Frequent interactions between the bubbles are observed especially at high gas contents. Collisions of adjacent bubbles and resulting phenomena such as coalescence and breakup are particularly observed near the free surface. In this area, a noticeable number of small bubbles form as a result of gas entrainment or bubble breakup. These smaller bubbles can be entrapped by the flow and transported into deeper zones of the liquid metal.

- The frequency of bubble injection is detected by analysing temporal changes of the image brightness along a horizontal measuring line at a certain distance from the gas injection point. The bubble injection frequencies found in our experiments are about a factor of two higher as comparable data reported for water. [6] In case of the bottom lance position the bubbling frequency remains almost constant within the range of gas flow rates investigated in this study. Counter-intuitively, measurements carried out for higher positions even show a slight decrease in frequency with increasing gas flow rate.

- The mean equivalent diameter of the injected bubbles increases with increasing gas flow rate. The bubble size histograms tend to show a bipolar distribution at sufficiently high gas flow rates which indicates a substantial amount of smaller gas bubbles. As already mentioned, these smaller bubbles are generated near the free surface by gas entrainment and bubble breakup. A sufficiently intense flow in the liquid metal ensures that the small bubbles remain suspended in the melt for longer times.

- The combination of high gas flow rates and a deep position of the top submerged lance produces the largest number of bubbles of various sizes and thus leads to an increase in the interfacial area. Such conditions should lead to high reaction rates in the case of a metallurgical reactor.

The experimental results obtained within this study provide a substantial database for the validation of respective numerical simulations. The work presented here is a first step in the systematic investigation of liquid metal multiphase flows in the TSL configuration. Continuing studies will extend the range of diverse experimental parameters taking into account a further increase of the gas flow rate, different nozzle geometries or variations of the material properties (viscosity). In addition, future experiments will also include the measurement of velocities of both the liquid metal and the gas bubbles.

Reference

1. J.M. Floyd: *Metall. Mater. Trans. B*, 2005, vol. 36, pp. 557–75.
2. B.U.N. Igwe, S. Ramachandran, and J.C. Fulton: *Metall. Trans.*, 1973, vol. 4, pp. 1887–94.
3. D. Mazumdar and R.I.L. Guthrie: *Metall. Trans. B*, 1985, vol. 16, pp. 83–90.
4. M. Iguchi, T. Uemura, H. Yamaguchi, T. Kuranaga, and Z. Morita: *ISIJ Int.*, 1994, vol. 34, pp. 973–9.

5. J. Wang, H. Ooyabu, F. Wang, and M. Iguchi: *ISIJ Int.*, 2011, vol. 51, pp. 1080–5.
6 . A. Gosset, P. Rambaud, P. Planquart, J.-M. Buchlin, E. Robert, L. Guo, D.D. Joseph, Y. Matsumoto, Y. Sommerfeld, and Y. Wang: Xi'an (China), 2010, pp. 205–10.
7. T. Goda, M. Iguchi, Y. Sasaki, and H. Kiuchi: *Mater. Trans.*, 2005, vol. 46, pp. 2461–6.
8. Y.S. Morsi, W. Yang, B.R. Clayton, and N.B. Gray: *Can. Metall. Q.*, 2000, vol. 39, pp. 87–98.
9. C.B. Solnordal, F.R.A. Jorgensen, and R.N. Taylor: *Metall. Mater. Trans. B*, 1998, vol. 29, pp. 485–492.
10. N. Huda, J. Naser, G. Brooks, M.A. Reuter, and R.W. Matusewicz: *Metall. Mater. Trans. B*, 2010, vol. 41, pp. 35–50.
11. N. Huda, J. Naser, G. Brooks, M.A. Reuter, and R.W. Matusewicz: *Metall. Mater. Trans. B*, 2012, vol. 43, pp. 39–55.
12. S. Torres and M.A. Barron: *Open J. Appl. Sci.*, 2016, vol. 06, pp. 860–7.
13. O. Keplinger, N. Shevchenko, and S. Eckert: *IOP Conf. Ser. Mater. Sci. Eng.*, 2017, vol. 228, p. 012009.
14. O. Keplinger, N. Shevchenko, and S. Eckert: *Int. J. Multiph. Flow*, 2018, vol. 105, pp. 159–69.
15. T. Vogt, S. Boden, A. Andruszkiewicz, K. Eckert, S. Eckert, and G. Gerbeth: *Nucl. Eng. Des.*, 2015, vol. 294, pp. 16–23.
16. G.N. Oryall and J.K. Brimacombe: *Metall. Trans. B*, 1976, vol. 7, pp. 391–403.
17. Y. Plevachuk, V. Sklyarchuk, S. Eckert, G. Gerbeth, and R. Novakovic: *J. Chem. Eng. Data*, 2014, vol. 59, pp. 757–63.
18. K. Timmel, N. Shevchenko, M. Röder, M. Anderhuber, P. Gardin, S. Eckert, and G. Gerbeth: *Metall. Mater. Trans. B*, 2015, vol. 46, pp. 700–710.
19. C. Tomasi and R. Manduchi: in *Sixth International Conference on Computer Vision (IEEE Cat. No.98CH36271)*, Narosa Publishing House, Bombay, India, 1998, pp. 839–46.
20. D. Bradley and G. Roth: *J. Graph. Tools*, 2007, vol. 12, pp. 13–21.
21. J. Serra: *Signal ProcesS-1*994, vol. 38, pp. 3–11.
22. E. Delnoij, J. Westerweel, N.G. Deen, J.A.M. Kuipers, and W.P.M. van Swaaij: *Chem. Eng. Sci.*, 1999, vol. 54, pp. 5159–71.
23. T. Sanada, M. Watanabe, T. Fukano, and A. Kariyasaki: *Chem. Eng. Sci.*, 2005, vol. 60, pp. 4886–900.
24. L. Liu, O. Keplinger, T. Ma, T. Ziegenhein, N. Shevchenko, S. Eckert, H. Yan, and D. Lucas: *Chem. Eng. Sci.*, 2018, vol. 192, pp. 288–305.
25. L. Liu, O. Keplinger, T. Ziegenhein, N. Shevchenko, S. Eckert, H. Yan, and D. Lucas: *Int. J. Multiph. Flow*, 2019, vol. 110, pp. 218–37.
26. M. Iguchi, T. Chihara, N. Takanashi, Y. Ogawa, N. Tokumitsu, and Z. Morita: *ISIJ Int.*, 1995, vol. 35, pp. 1354–61.
27. I. Leibson, E.G. Holcomb, A.G. Cacoso, and J.J. Jacmic: *AIChE J.*, 1956, vol. 2, pp. 300–6.

Supplementary Material

Video S1	Experimental video for a gas flow rate of Q_{gas} = 0.05 l/s at the top injection position
Video S2	Experimental video for a gas flow rate of Q_{gas} = 0.05 l/s at the middle injection position
Video S3	Experimental video for a gas flow rate of Q_{gas} = 0.05 l/s at the bottom injection position
Video S4	Experimental video for a gas flow rate of Q_{gas} = 0.1 l/s at the bottom injection position

Figure captions

Fig. 1 Schematic drawings of (a) the experimental setup and (b) the vessel and positions of the top submerged lance.

Fig.2 Consecutive steps of image processing leading to (a) a rescaled gray-scale image, (b) a bilaterally blurred image, (c) a binary image resulting from the adaptive thresholding, (d) a binary image after morphological transformation and, (e) a two-dimensional distribution of the local void fraction inside the bubble projection area.

Fig.3 Distribution of the gas phase in the fluid vessel for a gas flow rate of Q_{gas} = 0.05 l/s and the bottom injection position (L = 3/4 H): (a) rescaled gray-scale image, (b) binary image, (c) two-dimensional distribution of the local void fraction, (d) the probability of bubble presence $P(y, z)$ for an averaging period of one second, and (e) distribution of the time-averaged local void fraction for the same averaging period.

Fig.4 Sequences of rescaled images for a gas flow rate of Q_{gas} = 0.05 l/s for different submerged

depths of the nozzle: (a)-(c) L = 1/4 H (top), (d)-(f) L = 1/2 H (middle), and (g)-(i) L = 3/4 H (bottom).

Fig.5 Probability to detect a gas bubble (averaging period: 1 s) for a gas flow rate of Q_{gas} = 0.05 l/s and the bottom injection position (L = 3/4 H) at different points in time after onset of gas injection: (a) 1 s, (b) 4 s, and (c) 31 s, and for a gas flow rate of Q_{gas} = 0.1 l/s and the middle injection position (L = 1/2 H):(d) 1 s, (e) 4 s, and (f) 31 s.

Fig.6 Probability of bubble presence during a measurement time of 40 s for a gas flow rate of Q_{gas} = 0.05 l/s at three different lance submergence depths: (a) L = 1/4 H (top), (b) L = 1/2 H (middle), and (c) L = 3/4 H (bottom), and (d) for a gas flow rate of Q_{gas} = 0.1 l/s at L = 1/2 H (middle).

Fig.7 (a) Arrangement of the measurement line in the fluid layer, and (b) detail of the time series of the sum of intensities $S(t)$ along the measurement line at z = 20 mm for a gas flow rate of Q_{gas} = 0.05 l/s at the bottom injection position (L = 3/4 H) and (c) corresponding power spectrum of S(t) (the dashed line indicates the Gaussian fit).

Fig.8 Bubble injection frequency as a function of the gas flow rate Q_{gas} at three different injection positions.

Fig.9 Snapshots of the two-dimensional distribution of the local void fraction for different gas flow rates: (a) Q_{gas} = 0.033 l/s, (b) Q_{gas} = 0.066 l/s and (c) Q_{gas} = 0.1 l/s at the bottom injection position (L = 3/4 H).

Fig.10 Histograms of the average numbers of bubbles per frame for varying equivalent bubble diameters estimated by the projected area d_A and by the bubble volume d_V for different gas flow rates: (a, d) Q_{gas} = 0.033 l/s, (b, e) Q_{gas} = 0.066 l/s and (c, f) Q_{gas} = 0.1 l/s. All histograms show the data obtained for the bottom lance position (L = 3/4 H). The dashed line represents the threshold chosen for the minimum in the bubble size distributions.

Fig.11 Mean equivalent bubble diameter as a function of the gas flow rate Q_{gas} for the bottom lance position.

Fig.12 Variation of the injection Strouhal number as a function of the ratio of the Weber number to the Bond number (the dotted line represents the fit $St = 0.00048 \times (We/Bo)^{-0.70}$).

Table 1 – Comparison of experimental parameters Q_{gas}, u_{gas} and Re_l considered in [6] and in the present work.

	Q_{gas} [l/s]	u_{gas} [m/s]	Re_l
Gosset et al.[6] (d_{in} = 9 mm)	0.05 … 5	0.785 … 7.85	382 … 3820
this study (d_{in} = 5 mm)	0.033 … 0.1	1.68 … 5.09	700 … 2120